Spectral analysis of three-dimensional photonic jets

Alexis Devilez, Brian Stout, Nicolas Bonod, Evgeny Popov

Institut Fresnel, Aix-Marseille Université, CNRS
Domaine Universitaire de St Jérôme, 13397 Marseille, France
alexis.devilez@fresnel.fr

Abstract: The spatial and spectral properties of three-dimensional photonic jets are studied in a framework employing rigorous Lorentz-Mie theory. The contributions to the field from each spectral component are studied quantitatively and highlight the distinctive features of photonic jets. In particular, the role of evanescent field in photonic jets generated by small spheres is investigated. Secondary lobes in the propagative frequency distribution are also singled out as a distinctive property of photonic jets. It is shown that these differences lead to angular openings of photonic jets at least twice as small as those in comparable 'Gaussian' beams.

© 2008 Optical Society of America

OCIS codes: (230.3990) Micro-optical devices; (290.4020) Mie theory; (260.2110) Electromagnetic optics; (290.5850) Scattering, particles.

References and Links

1. Z. Chen, A. Taflove, and V. Backman, "Photonic nanojet enhancement of backscattering of light by nanoparticles: a potential novel visible-light ultramicroscopy technique," Opt. Express **12**, 1214-1220 (2004).
2. X. Li, Z. Chen, A. Taflove, and V. Backman, "Optical analysis of nanoparticles via enhanced backscattering facilitated by 3-D photonic nanojets," Opt. Express **13**, 526-533 (2005).
3. Z. Chen, A. Taflove, X. Li, and V. Backman, "Superenhanced backscattering of light by nanoparticles," Opt. Lett. **31**, 196-198 (2006).
4. A. Heifetz, K. Huang, A. V. Sahkian, X. li, A. Taflove, and V. Backman, "Experimental confirmation of backscattering enhancement induced by a photonic jet," Appl. Phys. Lett. **89**, 221118 (2006).
5. P. Ferrand, J. Wenger, M. Pianta, H. Rigneault, A. Devilez, B. Stout, N. Bonod, and E. Popov, "Direct imaging of photonic nanojet," Opt. Express **16**, 6930 - 6940 (2008).
6. D. Grojo, P. Delaporte, and A. Cros, "Removal of particles by impulsional laser," Journal de Physique IV **127**, 145-149 (2005).
7. S. M. Huang, M. H. Hong, B. Luk'yanchuk, and T. C. Chong, "Nanostructures fabricated on metal surfaces assisted by laser with optical near-field effects," Appl. Phys. A: Mater. Sci. Process. **77**, 293-296 (2003).
8. W. Guo, Z. B. Wuang, L. Li, D. J. Whitehead, B. S. Luk'yanchuk, and Z. Liu, "Near-field laser parallel nanofabrication of arbitrary-shaped patterns," Appl. Phys. Lett. **90**, 243101 (2007).
9. S. Lecler, S. Haacke, N. Lecong, O. Crégut, J. L. Rehspringer, and C. Hirlimann, "Photonic jet driven non-linear optics: example of two-photon fluorescence enhancement by dielectric microspheres," Opt. Express **15**, 4935-4942 (2007).
10. J. Kofler and N. Arnold, "Axially symmetric focusing as a cuspoid diffraction catastrophe: Scalar and vector cases and comparison with the theory of Mie," Phys. Rev. B **73**, 235401 (2006).
11. A. V. Itagi and W. A. Challener, "Optics of photonic nanojets," J. Opt. Soc. Am A **22**, 2847-2858 (2005).
12. B. Stout, M. Nevière, and E. Popov, "Light diffraction by three-dimensional object: differential theory," J. Opt. Soc. Am. A **22**, 2385-2404 (2005).
13. O. Moine and B. Stout, "Optical force calculations in arbitrary beams by use of the vector addition theorem," J. Opt. Soc. Am. B **22**, 1620-1631 (2005).
14. M. Born and E. Wolf, "Rigorous diffraction theory," in *Principles of optics*, M. Born and E. Wolf (Pergamon press, 1986), pp. 556-592.
15. M. Born and E. Wolf, "Optics of metals," in *Principles of optics*, M. Born and E. Wolf (Pergamon press, 1986), pp. 611-664.
16. L. Mandel and E. Wolf, "Some useful mathematical techniques," in *Optical coherence and quantum optics*, L. Mandel and E. Wolf (Cambridge University press, 1995), pp. 92-146.
17. H. C. Van de Hulst, "Very large spheres," in *Light scattering by small particles*, H. C. Van de Hulst (Dover publication, 1981), pp. 200-227.
18. W. J. Wiscombe, "Improved Mie scattering algorithms," Appl. Opt. **19**, 1505-1509 (1980).

19. M. Born and E. Wolf, "Elements of the theory of diffraction," in *Principles of optics*, M. Born and E. Wolf (Pergamon press, 1986), pp. 370-458.

1. Introduction

Scattering of light by microspheres is an old and well known problem, analytically solved a century ago by Mie. This classical problem has recently received renewed interest by Chen et al. who reported the existence of 'photonic jets' in FDTD calculations [1-3]. Their simulations showed that when illuminating cylinders [1] or spheres [2] with plane waves, one can produce narrow beams in the near field of the shadow-side surface. These beams typically have FWHM (Full Width at Half Maximum) widths smaller than the incident wavelength and remain subwavelength over distances of several wavelengths. Moreover, the intensity can be hundreds of times higher than the incident intensity [2]. The existence of photonic jets has since been experimentally confirmed in microwaves range [4], and directly observed in the optical waves range with a confocal microscope operating in detection mode [5].

The ability of microspheres to focus light and enhance the electromagnetic (EM) field was previously known and utilized to remove particles from a substrate in laser dry cleaning technique [6]. Arrays of particles-lenses were proposed in 2003 as a technique to pattern a substrate with neither mask nor lithographic processes [7]. This technique enables one to pattern various shapes by illuminating the array at different angles [8]. The subwavelength properties of photonic jets and the advent of nanosciences and biotechnology, recommend photonic jets as a useful tool for high resolution nano-particles detection [1-3], fluorescence microscopy improvements [9] and nanopatterning [7,8]. A fuller understanding of this beam is nevertheless needed to fully exploit the potential of microspheres as optical components.

An analytical study of light focusing by axially symmetric systems has been performed using wave propagation theory in systems having spherical aberrations, extending the geometrical optics approach [10]. The field is developed on high-order Bessoid integrals which are vectorial three-dimensional generalizations of the Pearsey Integral. Applied to microspheres, this formalism describes "photonic jets" as resulting from off-axis rays converging towards different points with different angles as a consequence of spherical aberrations. In this framework, photonic jets are approximated as Bessel beams of variable cross section. This description provides physical insights, tending towards Mie theory for size parameters above 30. For smaller spheres, the agreement is less accurate due in part to evanescent field contributions not taken into account in the geometric optics framework.

A spectral analysis of the photonic jets has previously been carried out by Itagi et al. [11] for cylinders. They concluded that the evanescent field only makes small contributions to photonic jets properties which are mainly due to a particular phase distribution. Chen et al. also affirmed that photonic jets do not involve evanescent fields [1], but this still need to be closely examined for spherical problems invoking a complete three-dimensional analysis.

In this work, numerical parameters are presented in section 2. The three dimensional spectral expansion of the field described in section 3, permits a quantitative analysis of the contribution of the different spatial frequencies in photonic jets field distributions in section 4. The propagation of photonic jets is then studied in section 5 where a comparison with Gaussian beam is made for didactic purposes.

2. Simulations parameters

Throughout this article, an incident wavelength in the optical range, $\lambda_v = 525$ *nm*, is adopted. At this wavelength, latex spheres have a refractive index of $N_s = 1.6$. The surrounding medium is considered to be either air, $N_0 = 1$, or water, $N_0 = 1.33$. The index contrast will then be respectively equal to $\rho = 1.6$, or $\rho = 1.2$. For a radius $R = 1$ *μm*, the corresponding size parameters are respectively $k_0R = 2\pi R N_0/\lambda_v = 12$ and $k_0R = 16$.

The intensity distribution (Hermitian square of the electric field) produced by a latex microsphere of radius 1 *μm* in water illuminated by a plane wave is simulated in Fig. 1(a).

The photonic jet can roughly be described with 4 parameters displayed in Fig. 1(b): the 'focal' distance f from the surface of the sphere to the point of maximum intensity, the intensity enhancement I_{max}, at the 'focus', the beam width w_0 at the focus and finally the 'diffraction length' z_r. These last two parameters will be precisely defined in the next paragraph analogously to Gaussian beam parameters.
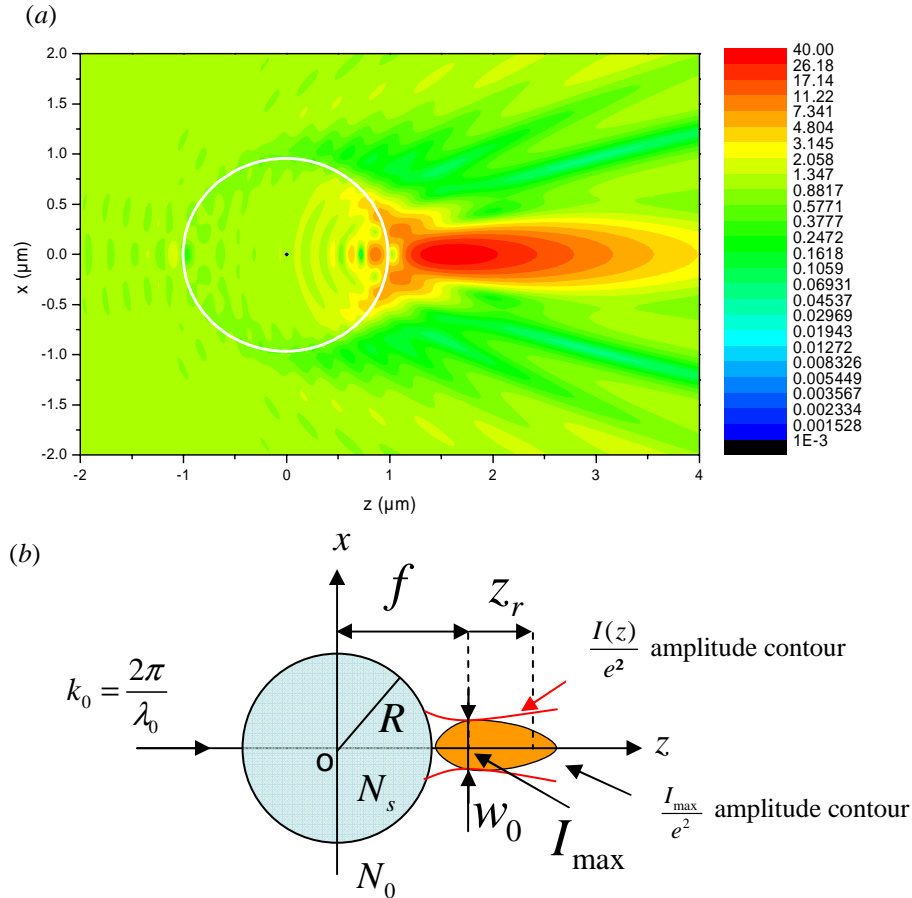
(a)

(b)

Fig. 1. Photonic jet produced when a dielectric sphere of radius $R = 1$ μm, and refractive index N_s is illuminated by a plane wave propagating along the z axis in a homogeneous embedding medium of refractive index N_0 ($\rho = N_s/N_0 = 1.2$, $\lambda_v = 525$ nm, $\lambda_0 = \lambda_v/N_0$, $k_0R = 16$). (a) A hot scale map of a photonic jet is displayed on a logarithmic scale of the electric field intensity. (b) A schema for photonic jet parameters is provided: 'focal' distance f , maximum enhancement I_{max} , width at f, w_0 and diffraction length z_r . The amplitude contours of the photonic jet at $I(z)/e^2$ and I_{max}/e^2 are also displayed.

The numerical code permits the calculation of the total and scattered field throughout all space when an incident field interacts with a microsphere. To characterize photonic jets, the intensity enhancement of the EM field has been displayed on two axes of interest: the propagation axis z and a transverse axis x at $z = f$. An example is presented in Fig. 2, for $R = 1$ μm and $\rho = 1.2$. It has been found that the intensity enhancement along the propagation axis z, displayed in Fig. 2(a), can be fitted in its decreasing part by a Lorentzian distribution. At the same time, the transversal intensity enhancement, displayed in Fig. 2(b) can be predominantly fitted by a Gaussian distribution. Therefore, we define the diffraction length, z_r , as the half width of the photonic jet at the half maximum of the Lorentzian fit of the axial intensity

distribution, and the beam width, $w(z)$ as the transverse width at $I(z)/e^2$ of the Gaussian fitted distribution. The width at the diffraction focus, w_0, of the photonic jet is then defined as the width at $z = f$.
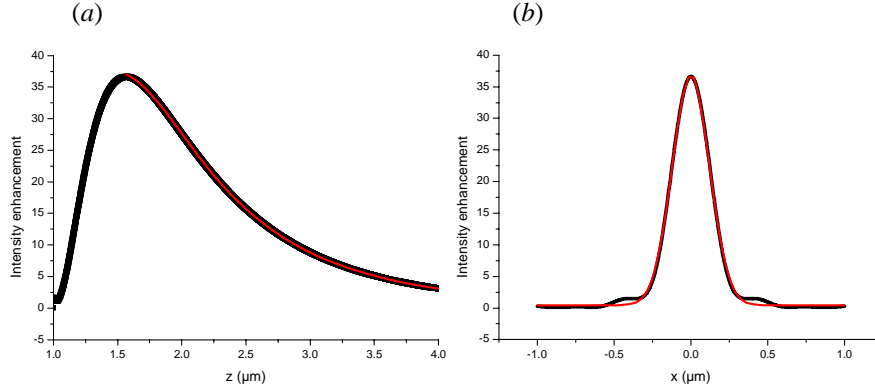

Fig. 2. Intensity enhancement distribution for a 1 μm radius sphere illuminated by a plane wave at $\lambda_v = 525$ nm with an index contrast of $\rho = 1.2$, $\lambda_0 = \lambda_v/N_0 = 394$ nm (*a*) along the propagation axis (z) (in black), and its Lorentzian fit (in red), $z_r = 800$ nm (*b*) along a transverse axis (x) for $z = f = 1.57$ μm (in black), and its Gaussian fit (in red), $w_0 = 241$ $nm = 0.6\lambda_0$.

Despite these similarities with Gaussian beam distributions, it can be argued [10] that photonic jets are more accurately described in terms of Bessel beams of variable cross sections [10]. However, Gaussian beams are generated by classical optical devices, and commonly encountered in experiments. This comparison can lead to a practical understanding of photonic jet properties. As could be expected, photonic jets nevertheless differ from Gaussian beams, especially with respect to the way in which they propagate. The study of the spatial frequencies involved in the photonic jets field distribution will be particularly useful in distinguishing photonic jets from Gaussian beams.

3. Spectral study of photonic jets

A rigorous angular spectral analysis of the scattered field is performed here by expanding the partial waves on plane waves [14-16] to calculate the EM field. In Lorentz-Mie theory, the scattered field is expanded on a set of Vector Spherical Wave Functions (VSWFs), commonly denoted $\mathbf{M}_{n,m}$ and $\mathbf{N}_{n,m}$ [12,13]:

$$\mathbf{E}_{\mathrm{scat}}(r,\theta,\phi) = E_0 \sum_{n=1}^{\infty} \sum_{m=-n}^{n} f_{n,m}^{(h)} \mathbf{M}_{n,m}(k_0 r,\theta,\phi) + f_{n,m}^{(e)} \mathbf{N}_{n,m}(k_0 r,\theta,\phi) \quad (1)$$

where $f_{n,m}$ are the Mie coefficients for scattered field and $k_0 = 2\pi N_0/\lambda_v$ is the propagation wave vector in the host medium. The details of our notations are given in Appendix A. Expressing the transverse wavevector $\vec{\mathbf{K}}$ as:

$$\vec{\mathbf{K}} = K\cos\phi_k \hat{\mathbf{x}} + K\sin\phi_k \hat{\mathbf{y}}, \quad (2)$$

one can write a spectral decomposition of the outgoing VSWFs in the form:

$$\mathbf{M}_{n,m}(k_0 r_{//},\phi,z) = \int_{K=0}^{\infty}\int_{\phi=0}^{2\pi} \mathbf{X}_{n,m}(\theta_k,\phi_k)\frac{e^{i(\vec{K}.\vec{r}_{//}+k_z|z|)}}{k_z}KdKd\phi_k$$

$$\mathbf{N}_{n,m}(k_0 r_{//},\phi,z) = \int_{K=0}^{\infty}\int_{\phi=0}^{2\pi} \mathbf{Z}_{n,m}(\theta_k,\phi_k)\frac{e^{i(\vec{K}.\vec{r}_{//}+k_z|z|)}}{k_z}KdKd\phi_k \quad (3)$$

where ($r_{//}$, ϕ, z) are cylindrical coordinates and $k_z = \sqrt{k_0^2 - K^2}$. One can observe that the VSWFs can be interpreted as the angular spectrum in the plane wave representation of the

vector spherical harmonics. Spectral decompositions were here and henceforth restricted to the scattered field since they are unsuitable for describing incident plane waves (which are represented by a Dirac distributions at $K = 0$).

To proceed further, we adopt the simplifying case of a sphere illuminated by a circularly right-polarized incident plane wave so that the field is entirely described by VSWFs with $m = 1$ (arbitrary polarization can of course be obtained by superpositions with circularly left polarized waves, $m = -1$). Using the Cartesian vector spherical harmonics, the scattered field can be written as:

$$\mathbf{E}_{\text{scat}}(r_{//}, \phi, z) = E_0 \int_0^\infty \frac{K}{k_0} d\frac{K}{k_0} \begin{bmatrix} A(\frac{K}{k_0}, \phi, z) J_0(Kr_{//}) \frac{\{\hat{\mathbf{x}}+i\hat{\mathbf{y}}\}}{\sqrt{2}} \\ B(\frac{K}{k_0}, \phi, z) J_1(Kr_{//}) \hat{\mathbf{z}} \\ C(\frac{K}{k_0}, \phi, z) J_2(Kr_{//}) \frac{\{\hat{\mathbf{x}}-i\hat{\mathbf{y}}\}}{\sqrt{2}} \end{bmatrix} \text{ with } \begin{array}{l} A = \sum_{n=0}^\infty f_n^{(h)} A_n^{(h)} + f_n^{(e)} A_n^{(e)} \\ B = \sum_{n=0}^\infty f_n^{(h)} B_n^{(h)} + f_n^{(e)} B_n^{(e)} \\ C = \sum_{n=0}^\infty f_n^{(h)} C_n^{(h)} + f_n^{(e)} C_n^{(e)} \end{array} \quad (4)$$

where details and full expressions are relegated to Appendix B. This expansion provides the angular spectrum of plane waves representation of the field via three different coefficient functions, A, B, and C. We focus our attention on the total spectral amplitude $S = (AA^*+BB^*+CC^*)^{1/2}$.

The total spectral amplitude is presented in Fig. 3 as a function of the normalized radial spatial frequencies K/k_0 for a sphere of radius $R = 1$ μm at the position $\phi = 0$, $z = 1.05$ μm. S is normalized to 1 at $K = 0$, and plotted for two different index contrasts $\rho = 1.2$ in Fig. 3(a) and $\rho = 1.6$ in Fig. 3(b). The radial spectrum has the following features: a generally decreasing and oscillating features in the region $0 < K/k_0 < 1$ corresponding to propagative fields, a singularity originating from the homogeneous medium Green function at $K/k_0 = 1$ and a monotonically decreasing behaviour when $K > k_0$ for evanescent field contributions.
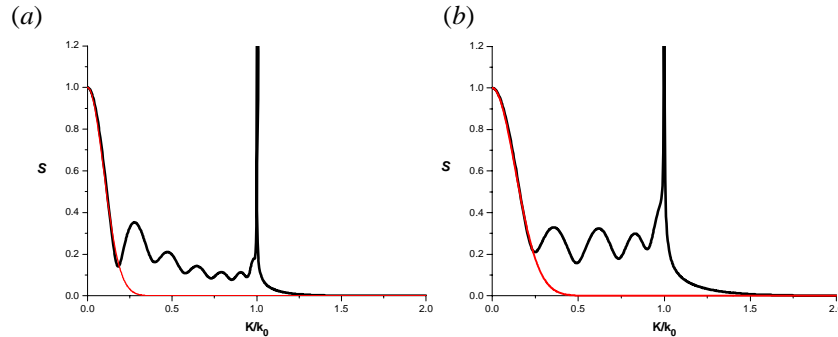
(a)   (b)

Fig. 3. Total spectral amplitude $S = (AA^*+BB^*+CC^*)^{1/2}$ as a function of normalized spatial frequencies K/k_0 at $z = 1.05$ μm, for a sphere of radius $R = 1\mu m$, and index contrasts (a) $\rho = 1.2$ and (b) $\rho = 1.6$, illuminated by a plane wave at $\lambda_v = 525$ nm. The low frequencies are respectively fitted by a Gaussian frequency distribution of respective widths $K/k_0 = 0,190$ in (a) and $K/k_0 = 0,270$ in (b) (red line).

The propagative frequency decomposition can be separated in two regions of interest. From the zero-frequency to the first minimum, the spectral distribution can be described by a narrow Gaussian-type distribution. The secondary maxima and minima which can be observed in the higher spatial propagative frequencies enrich the jet spectrum. These secondary maxima result in photonic jets having features that differ from Gaussian beams in direct space. By comparing Fig. 3(b) with Fig. 3(a), one can see that higher index contrast enhances the high spatial frequency components which results in a stronger focalization and a narrower photonic jet [10, 16].

One can also deduce from Fig. 3 that the strength of the evanescent field contribution depends significantly on the refraction index contrast and position at which the spectral decomposition is carried out. This dependence is highlighted in Fig. 4, which displays a hot scale map of S as a function of the position along the propagation axis z and the radial frequencies K/k_0 for refraction index contrasts $\rho = 1.2$ in (a) and $\rho = 1.6$ in (b). For both index contrasts, the evanescent field is considerably attenuated after distances of more than 500 *nm*. Consequently, for low index contrasts, like $\rho = 1.2$ where $f = 1.6\ \mu m$, the evanescent field will not bring any significant contribution to the width properties of the photonic jet. On the other hand, for $\rho = 1.6$, the photonic jet is on the surface of the sphere so that contribution of the evanescent field may be important. This point and the influence of the high propagative spatial frequencies will be discussed in the next section.
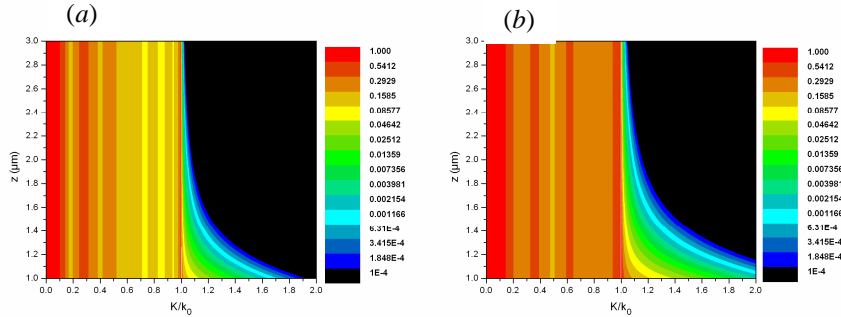

Fig. 4. S as a function of z and K/k_0 in logarithmic scale with the same parameters as used in Fig. 3(a) and Fig. 3(b) respectively.

In this section we have presented a rigorous analytical spectral expansion of three dimensional photonic jets. The next section will demonstrate how this tool can help in analyzing the properties of photonic jets and bring new elements to the understanding of the unique features of photonic jets in direct space.

4. Photonic jet analysis

4.1 Direct space analysis of evanescent and propagative spectral contributions

Using the spectral expansion of Eq. (4), one can plot the spatial distribution after having explicitly filtered out all evanescent (i.e. $K > k_0$) contributions. The photonic jet intensity along the propagation axis is plotted in red in Fig. 5(a)) while the intensity with the evanescent field removed is plotted in green. The same procedure is studied in Fig. 5(b)) for the transverse intensity at $z = f$. One remarks that when the evanescent field is removed, the maximum intensity position of the photonic jet moves away from the surface, the maximum field enhancement drops by half its value and the size of the width at diffraction focus is increased by 10 percent (from 230 *nm* to 256 *nm*). This example demonstrates that the evanescent field plays a significant role in the field distribution of photonic jets close to the surface of the sphere, which is the case when index contrasts are large. Nevertheless, the evanescent field cannot be held responsible for the principal photonic jet features, particularly when refractive index contrast is low.
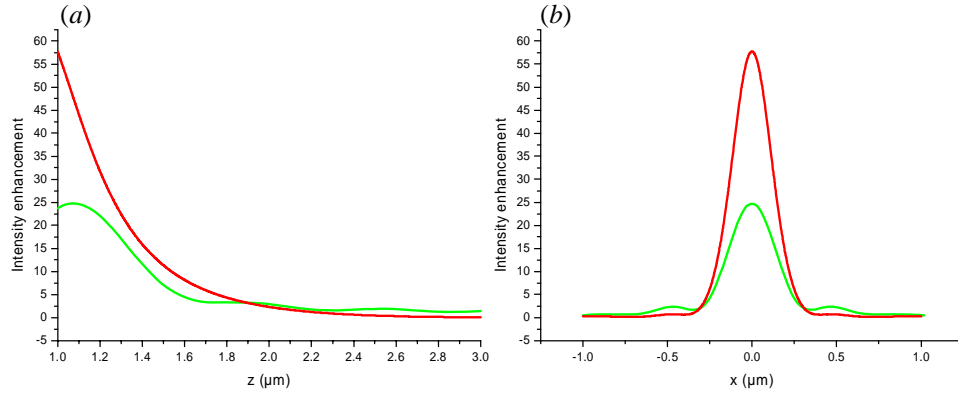
Fig. 5. Intensity distribution of the electric field: (*a*) along the propagation axis (*z*), and (*b*) at *z* = *f*, for sphere of radius *R* = 1μ*m* illuminated at λ_v = 525 *nm* for an index contrast of ρ = 1.6. The red curve corresponds to the full intensity while the green curve is the intensity once the evanescent field has been removed.

The spectral expansion of the previous section showed a rich structure in the high spatial frequency components of the photonic jet. In direct space, each propagative spatial frequency corresponds to propagation at a given angle with respect to the beam axis. An intensity map of a photonic jet is presented on a colored map in Fig. 6 (with ρ = 1.6). It shows the angles corresponding to the first few maxima (red) and the minima (black) of *S* (cf. Fig. 3(b)). The maxima correspond to high intensity angles while the minima correspond to angles of low intensity regions. The maxima in the spectral distribution can therefore be associated with the presence of secondary lobes in the direct field structure. The first secondary lobes tend to confine the central lobe into a low divergent beam, while the secondary lobes with high transverse components tend to reduce the length and the width of photonic jets.
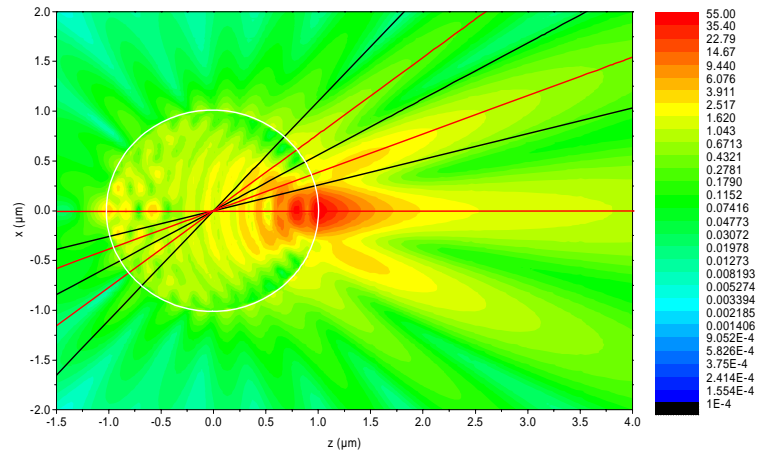

Fig. 6. Scattered intensity of a photonic jet produced by a sphere of radius 1 μ*m*, illuminated at λ_v = 525 *nm* with an index contrast of ρ = 1.6. The angles corresponding to the maxima and minima in the spatial frequency expansion of Fig. 3(b) are displayed in direct space by red lines and black lines respectively.

The properties of the field scattered by a microsphere illuminated by a plane wave has been studied without including the incident field. The incident field contributions to the principal beam (i.e. photonic jet) are actually rather weak, except in the case of low index contrasts where they reduce the Rayleigh length. It will however be demonstrated in section 5

that the 'total' photonic jets still can have particularly low angular openings when index contrasts are low. Therefore, the restriction to the study of the scattered field spectrum appears sufficient to highlight the distinctive physical properties of photonic jets.

4.2 Origin of the secondary lobes

The origin of secondary lobes illustrated in Fig. 6 can be found in the spherical geometry of the microspheres and the corresponding spherical geometry of VSWFs (or multipolar waves) which are eigenmodes of the spherical Maxwell propagation equation. The amplitude of the scattered field coefficients, $|f^{(h)}_{n,1}|$ and $|f^{(e)}_{n,1}|$ in this expansion are displayed in Fig. 7, where we recall that scattered field in the VSWF basis is expressed:

$$\mathbf{E}_{\text{scat}}(r,\theta,\phi) = E_0 \sum_{n=1}^{\infty} \sum_{m=-n}^{n} f^{(h)}_{n,m}\mathbf{M}_{n,m}(k_0 r,\theta,\phi) + f^{(e)}_{n,m}\mathbf{N}_{n,m}(k_0 r,\theta,\phi) \tag{5}$$
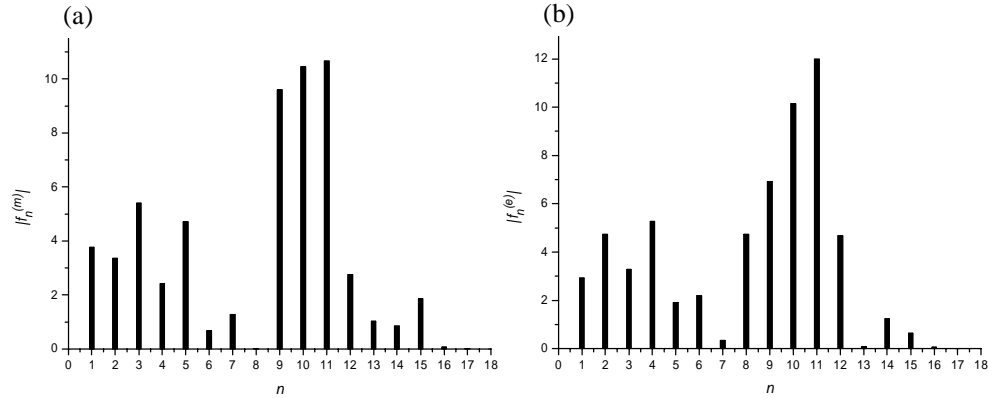
(a)

(b)

Fig. 7. Amplitude of scattered coefficients of photonic jets in the VSWF expansion; (a) for the magnetic $|f^{(h)}_{n,1}|$ coefficients, (b) for the electric $|f^{(e)}_{n,1}|$ coefficients. $R = 1\mu m$, $\rho = 1.6$, $\lambda_v = 525$ nm.

Figure 7 illustrates that photonic jets can be seen as finite linear superpositions of high order VSWF, used to describe the EM field in the context of a rigorous EM theory. It can be noticed that the predominant order n is approximatively equal to the size parameter kR. This corresponds to rays passing close to the edge of the sphere in the context of Van de Hulst's localization principle [17]. The scattered intensity of the term of VSWFs of order $n = 11$, which slightly dominates is displayed in Fig. 8. $|f^{(h)}_{11} \mathbf{M}_{11,1}|^2$ is displayed in Fig. 8(a) and $|f^{(e)}_{11} \mathbf{N}_{11,1}|^2$ in Fig. 8(b). The VSWFs waves have intensity distributions comprised of number of 'beams' (there are in fact $2n$ 'beams' in a VSWF of order n). The secondary beams seen in Figs. 1 and 6 are therefore intrinsically present in the VSWFs.
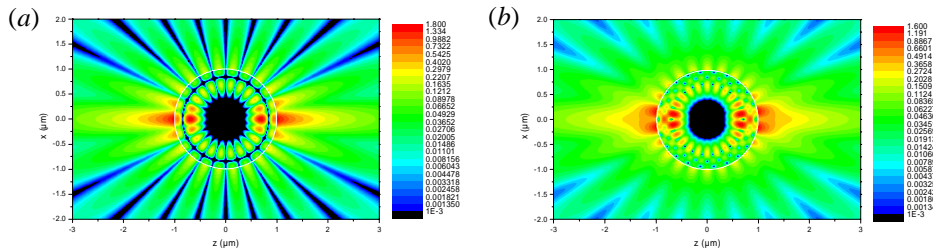
(a)

(b)

Fig. 8. Scattered intensity of the terms of order $n = 11$, (a) $|f^{(h)}_{11} \mathbf{M}_{11,1}|^2$, (b) $|f^{(e)}_{11} \mathbf{N}_{11,1}|^2$. $R = 1\mu m$, $\rho = 1.6$, $\lambda_v = 525$ nm.

The superposition of the principal order of this photonic jet, $n = 11$ (cf. Fig. 7) is displayed in Fig. 9.

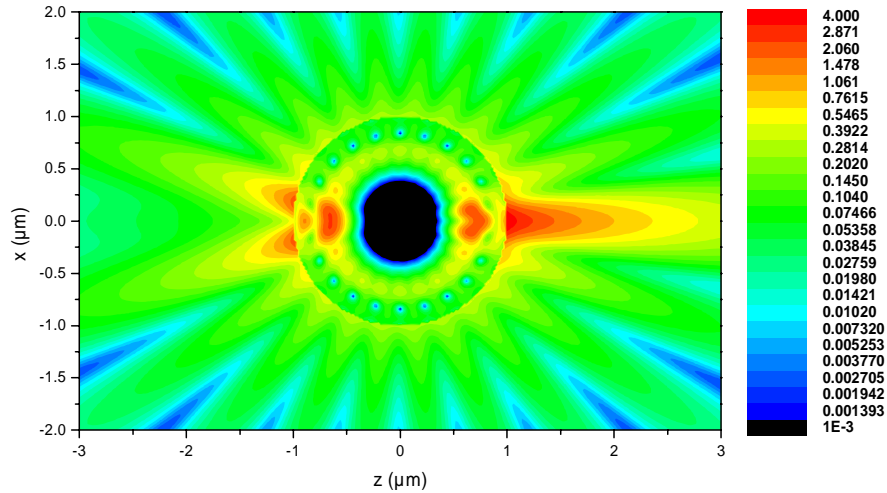
Fig. 9. Scattered intensity in $\log_{10}$ hot scale of a "photonic jet" generated with the principal order in the VSWF expansion: $n = 11$, i.e. $\left| f_{11}^{(h)} \mathbf{M}_{11,1} + f_{11}^{(e)} \mathbf{N}_{11,1} \right|^2$. $R = 1\ \mu m$, $\rho = 1.6$, $\lambda_v = 525\ nm$

One can see from Fig. 9 that the finite superposition of the multipolar waves of different type (**M** and **N**) tends to enhance the principal (forward direction) beam and reduce the intensity of the secondary beams, especially in the backward direction. However, the forward secondary lobes still contain non negligible intensity.

In this section, the electromagnetic origin of the photonic jet has been demonstrated. The secondary beams emerge as a natural consequence of the geometry and the scale ($\lambda \sim R$) of the scatterers which requires an expansion on VSWFs. These secondary beams thus appear as the principal distinguishing feature of photonic jets with respect to the Gaussian beam behaviour generated in a paraxial optics approximation.

5. Photonic jet propagation

The study of photonic jet spectrum in the previous sections has highligthed a narrow Gaussian-like fundamental contribution and oscillatory high spatial frequencies. As it is illustrated in Fig. 6, angular openings of photonic jets are linked with the width of this fundamental distribution. This single narrow fundamental Gaussian distribution would give rise in direct space to a weakly focused Gaussian beam, with low angular openings. In the Gaussian beam model, the beam waist w_0, and diffraction length z_r are linked by the relation $2z_r = k_0 w_0^2$. According to this formula, low angular openings $\theta_d \approx w_0/z_r$ are obtained for large waists. But, it has been observed that the principal beam (i.e. the photonic jet) is extremely narrow (cf Fig. 2). This fact is explained by the presence of oscillatory high spatial frequencies which enrich the angular spectrum and confine the field transversally. Using similarities with Gaussian beam of section 1, longitudinal confinement of photonic jets and Gaussian beams have been compared. For low index contrasts, it has been calculated that for identical waists, photonic jets present a Rayleigh length twice greater than classical Gaussian beams. Thus, its angular opening can be estimated to be twice lower than the Gaussian one. The oscillatory high spatial frequencies permit to generate a gaussian-like principal beams with low angular openings and extreme transversal confinement. A microsphere can easily create narrow beams with angular openings at least twice smaller than for a Gaussian beam

created by current high numerical aperture optical lenses. This confirms what was observed in the reciprocal space in previous sections. The beam created by a microsphere illuminated by an optical plane wave has a rich spectrum, leading to unique propagation features in direct space.

6. Conclusion

A three dimensional spectral analysis demonstrating the rich structure of photonic jets has been performed. This permits the study of the contributions from all spatial frequency components (both propagative and evanescent). This decomposition indicates predominantly propagative wave contributions, whose low frequency components are considered as a Gaussian type together with high spatial frequency components corresponding to secondary lobes in direct space. The evanescent field contributions to photonic jets created by microspheres have been demonstrated to play an important role, enhancing and sharpening the photonic jets field distribution, but not particularly involved in the low angular opening properties of photonic jets. It has been shown that the highly collimated photonic jets observed with low index contrast spheres is due to the presence of the secondary beams associated with the multipole nature of electromagnetic field interacting with microsphere. When the same sphere is embedded in air, the higher index contrast produces a more localized beam both in the radial and in the longitudinal directions. The fact that such simple and inexpensive optical components as dielectric microspheres provide beams of such unique and potentially useful properties opens up numerous perspectives for applications.

Appendix A: Numerical simulations

Home developed numerical codes based on Mie theory are used to perform the study. In this context, the electromagnetic field is expanded on the vector partial waves (also called the Vector Spherical Wave Functions VSWFs), commonly denoted $\mathbf{M}_{n,m}$ and $\mathbf{N}_{n,m}$ [12] :

$$\mathbf{M}_{n,m}(k_0 r, \theta, \phi) = h_n^{(+)}(k_0 r) \mathbf{X}_{n,m}(\theta, \phi)$$

$$\mathbf{N}_{n,m}(k_0 r, \theta, \phi) = \frac{1}{k_0 r}\left[h_n^{(+)}(k_0 r) \mathbf{Y}_{n,m}(\theta, \phi) + \left(k_0 r\, h_n^{(+)}(k_0 r)\right)' \mathbf{Z}_{n,m}(\theta, \phi) \right] \tag{6}$$

where $k_0 = 2\pi N_0/\lambda_v$ where λ_v is the incident vacuum wavelength and N_0 is the refractive index of the surrounding medium. The $\mathbf{Y}$, $\mathbf{Z}$, and $\mathbf{X}$ in eq.(1) are vector spherical harmonics (VSHs) defined in spherical coordinates by [13] as:

$$\mathbf{Y}_{n,m}(\theta, \phi) \equiv \hat{\mathbf{r}}\, Y_{n,m}(\theta, \phi)$$

$$\mathbf{Z}_{n,m}(\theta, \phi) \equiv \frac{r\nabla \mathbf{Y}_{n,m}(\theta, \phi)}{\sqrt{n(n+1)}} \tag{7}$$

$$\mathbf{X}_{n,m}(\theta, \phi) \equiv \mathbf{Z}_{n,m}(\theta, \phi) \times \hat{\mathbf{r}}$$

Singularity free partial waves are obtained by taking the regular part, denoted Rg, wherein the outgoing spherical Hankel functions h_n are replaced by spherical Bessel functions, j_n:

$$Rg\left\{\mathbf{M}_{n,m}(k_0 r, \theta, \phi)\right\} = j_n(k_0 r) \mathbf{X}_{n,m}(\theta, \phi)$$

$$Rg\left\{\mathbf{N}_{n,m}(k_0 r, \theta, \phi)\right\} = \frac{1}{k_0 r}\left[j_n(k_0 r) \mathbf{Y}_{n,m}(\theta, \phi) + \left(k_0 r\, j_n(k_0 r)\right)' \mathbf{Z}_{n,m}(\theta, \phi) \right] \tag{8}$$

These regular partial wave vectors are used to expand the incident and the internal field:

$$\mathbf{E}_{\mathrm{inc}}(r, \theta, \phi) = E_0 \sum_{n=1}^{\infty}\sum_{m=-n}^{n} a_{n,m}^{(h)} Rg\left\{\mathbf{M}_{n,m}(k_s r, \theta, \phi)\right\} + a_{n,m}^{(e)} Rg\left\{\mathbf{N}_{n,m}(k_s r, \theta, \phi)\right\}$$

$$\mathbf{E}_{\mathrm{int}}(r, \theta, \phi) = E_0 \sum_{n=1}^{\infty}\sum_{m=-n}^{n} s_{n,m}^{(h)} Rg\left\{\mathbf{M}_{n,m}(k_s r, \theta, \phi)\right\} + s_{n,m}^{(e)} Rg\left\{\mathbf{N}_{n,m}(k_s r, \theta, \phi)\right\} \tag{9}$$

where $k_s = 2\pi N_s/\lambda_v = \rho k_0$ and N_s the refractive index of the sphere with $\rho = N_s/N_0 = k_s/k_0$ the refractive index contrast. The a_{nm} and s_{nm} are respectively the incident and internal coefficients in the field expansion. E_0 is a real parameter determining the incident field amplitude. For plane waves, these coefficients are:

$$a_{n,m}^{(h)} = 4\pi i^n \mathbf{X}_{n,m}^*(\theta,\phi).\hat{\mathbf{e}}_i$$
$$a_{n,m}^{(e)} = 4\pi i^{n-1} \mathbf{Z}_{n,m}^*(\theta,\phi).\hat{\mathbf{e}}_i \qquad (10)$$

where $\hat{\mathbf{e}}_i$ is the incident field polarization. The EM wave is circularly polarized to facilitate the analysis:

$$\hat{\mathbf{e}}_i = \frac{\hat{\mathbf{x}} + i\hat{\mathbf{y}}}{\sqrt{2}} \qquad (11)$$

This choice renders the intensity axi-symmetric so that intensity maps in different planes are equivalent. The scattered field is expanded on the partial wave vectors:

$$\mathbf{E}_{scat}(r,\theta,\phi) = E_0 \sum_{n=1}^{\infty} \sum_{m=-n}^{n} f_{n,m}^{(h)} \mathbf{M}_{n,m}(k_0 r,\theta,\phi) + f_{n,m}^{(e)} \mathbf{N}_{n,m}(k_0 r,\theta,\phi) \qquad (12)$$

where $f_{n,m}$ are the scattered coefficients in the field expansion. The boundary conditions at the surface of the sphere, $r = R$, enable one to link the scattered field coefficients with the incident field coefficients via the 'Mie' coefficients:

$$f_{n,m}^{(h)} = \frac{\psi_n'(k_0 R)\psi_n(k_s R) - \rho\psi_n'(k_s R)\psi_n(k_0 R)}{\rho\xi_n'(k_0 R)\psi_n(k_s R) - \psi_n'(k_s R)\xi_n(k_0 R)} a_{n,m}^{(h)}$$

$$f_{n,m}^{(e)} = \frac{\psi_n'(k_s R)\psi_n(k_0 R) - \rho\psi_n'(k_0 R)\psi_n(k_s R)}{\rho\xi_n'(k_0 R)\psi_n(k_s R) - \psi_n'(k_s R)\xi_n(k_0 R)} a_{n,m}^{(e)} \qquad (13)$$

where $\psi_n(x) \equiv x j_n(x)$ and $\xi_n(x) \equiv x h_n^{(+)}(x)$ are the Ricatti Bessel functions. The 'Mie' coefficients only depend on the size parameter $k_0 R$ and the refractive index contrast between the two media, ρ. It is usually sufficient to adopt the Wiscombe criterion for the truncation of convergence of numerical simulations as a limit for the truncation of the basis [18].

Appendix B: Spectral expansion of the electromagnetic field

The spectral expansion of the EM field distribution of photonic jets can be obtained via an integral expansion of the VSWFs on a cylindrical coordinates and invoking Clebsch Gordan coefficients. In the Lorentz-Mie theory, the scattered EM field is expanded on the basis of VSWFs:

$$\mathbf{E}_{scat}(r,\theta,\phi) = E_0 \sum_{n=1}^{\infty} \sum_{m=-n}^{n} f_{n,m}^{(h)} \mathbf{M}_{n,m}(k_0 r,\theta,\phi) + f_{n,m}^{(e)} \mathbf{N}_{n,m}(k_0 r,\theta,\phi) \qquad (14)$$

where

$$\mathbf{M}_{n,m}(k_0 r,\theta,\phi) = h_n^{(+)}(k_0 r)\mathbf{X}_{n,m}(\theta,\phi)$$
$$\mathbf{N}_{n,m}(k_0 r,\theta,\phi) = \frac{1}{k_0 r}\left[h_n^{(+)}(k_0 r)\mathbf{Y}_{n,m}(\theta,\phi) + \left(k_0 r h_n^{(+)}(k_0 r)\right)' \mathbf{Z}_{n,m}(\theta,\phi) \right] \qquad (15)$$

and $\mathbf{X}_{n,m}$, $\mathbf{Y}_{n,m}$ and $\mathbf{Z}_{n,m}$ are the vector spherical harmonics and h_n is the spherical outgoing Hankel function. E_0 is a real parameter determining the incident field amplitude. It can be shown in the scalar case that:

$$h_n(k_0 r)Y_{n,m}(\hat{r}) = \frac{1}{2\pi i^n k_0} \int_{K=0}^{\infty} \int_{\phi_k=0}^{2\pi} K dK d\phi_k Y_{n,m}(\hat{k}) \frac{e^{\pm i\vec{k}.\vec{r}}}{k_z} \qquad \text{sign}(z) = \pm \qquad (16)$$

where $k_z = \sqrt{k_0^2 - K^2}$. $Y_{n,m}$ are the scalar spherical harmonics set as :

$$Y_{n,m}(\theta,\phi) = c_{n,m} P_n^m(\cos\theta) e^{im\phi} \tag{17}$$

where P_n^m are the associated Legendre polynomials and $c_{n,m}$ is a normalization factor:

$$c_{n,m} = \left[\frac{2n+1}{4\pi} \frac{(n-m)!}{(n+m)!} \right]^{1/2} \tag{18}$$

Using the spherical unit vectors:

$$\hat{\boldsymbol{\chi}}_{-1} = \frac{\hat{\mathbf{x}} - i\hat{\mathbf{y}}}{\sqrt{2}}, \quad \hat{\boldsymbol{\chi}}_0 = \hat{\mathbf{z}}, \quad \hat{\boldsymbol{\chi}}_1 = -\frac{\hat{\mathbf{x}} + i\hat{\mathbf{y}}}{\sqrt{2}} \tag{19}$$

where $\hat{x}$, $\hat{y}$, $\hat{z}$ are the cartesian unit vectors, and using the Cartesian vector spherical harmonics defined by:

$$\mathbf{Y}_{n,l}^m = \sum_{\mu=-1}^{1} (l,m-\mu;1,\mu \mid n,m) Y_{l,m-\mu} \hat{\boldsymbol{\chi}}_\mu \tag{20}$$

where $(l,m-\mu;1,\mu \mid n,m)$ are the Clebsch-Gordan coefficients, the vectorial spherical harmonics can be written in terms of cartesian spherical harmonics as:

$$
\begin{aligned}
\mathbf{X}_{n,m} &= \frac{\mathbf{Y}_{n,n}^m}{i} \\
\mathbf{Y}_{n,m} &= \sqrt{\frac{n}{2n+1}} \mathbf{Y}_{n,n-1}^m + \sqrt{\frac{n+1}{2n+1}} \mathbf{Y}_{n,n+1}^m \\
\mathbf{Z}_{n,m} &= \sqrt{\frac{n+1}{2n+1}} \mathbf{Y}_{n,n-1}^m - \sqrt{\frac{n}{2n+1}} \mathbf{Y}_{n,n+1}^m
\end{aligned}
\tag{21}
$$

The vector function analogue of eq. (15) is:

$$
\begin{aligned}
\mathbf{M}_{n,m}(k_0 r_{//},\phi,z) &= \int_{K=0}^{\infty} \int_{\phi=0}^{2\pi} \mathbf{X}_{n,m}(\theta_k,\phi_k) \frac{e^{i(\overline{K}\cdot\overline{r}_{//} + k_z|z|)}}{k_z} K dK d\phi_k \\
\mathbf{N}_{n,m}(k_0 r_{//},\phi,z) &= \int_{K=0}^{\infty} \int_{\phi=0}^{2\pi} \mathbf{Z}_{n,m}(\theta_k,\phi_k) \frac{e^{i(\overline{K}\cdot\overline{r}_{//} + k_z|z|)}}{k_z} K dK d\phi_k
\end{aligned}
\tag{22}
$$

The exponential part can be expanded as :

$$e^{i\mathbf{K}\cdot\mathbf{r}_{//}} = e^{iKr_{//}\cos(\phi_k - \phi)} \tag{23}$$

The integral according to ϕ_k can be analytically calculated using [19]

$$\int_0^{2\pi} e^{ix\cos(\phi_k - \phi)} e^{in\phi_k} d\phi_k = 2\pi i^n J_n(x) e^{in\phi} \tag{24}$$

Where J_n are the cylindrical Bessel functions

Proceeding further, we obtain:

$$\mathbf{E}_{\text{scat}}(r_{//},\phi,z) = E_0 \sum_{n=1}^{\infty} \int_0^{\infty} \frac{K}{k_0} d\frac{K}{k_0} f_n^{(h)} \begin{bmatrix} A_n^{(h)}(\frac{K}{k_0},\phi,z) J_0(Kr_{//}) \frac{\{\hat{\mathbf{x}}+i\hat{\mathbf{y}}\}}{\sqrt{2}} \\ B_n^{(h)}(\frac{K}{k_0},\phi,z) J_1(Kr_{//}) \hat{\mathbf{z}} \\ C_n^{(h)}(\frac{K}{k_0},\phi,z) J_2(Kr_{//}) \frac{\{\hat{\mathbf{x}}-i\hat{\mathbf{y}}\}}{\sqrt{2}} \end{bmatrix} + f_n^{(e)} \begin{bmatrix} A_n^{(e)}(\frac{K}{k_0},\phi,z) J_0(Kr_{//}) \frac{\{\hat{\mathbf{x}}+i\hat{\mathbf{y}}\}}{\sqrt{2}} \\ B_n^{(e)}(\frac{K}{k_0},\phi,z) J_1(Kr_{//}) \hat{\mathbf{z}} \\ C_n^{(e)}(\frac{K}{k_0},\phi,z) J_2(Kr_{//}) \frac{\{\hat{\mathbf{x}}-i\hat{\mathbf{y}}\}}{\sqrt{2}} \end{bmatrix}$$

$$(25)$$

Where we assume that the plane wave is circularly right polarized so that only $\mathbf{M}_{n,1}(k_0 r_{//}, \phi, z)$ and $\mathbf{N}_{n,1}(k_0 r_{//}, \phi, z)$ contribute to the field expansion and

$$A_n^{(h)} = \frac{-1}{i^{n+1}}(n,0;1,1\,|\,n,1)c_{n,0}P_n^0(\sqrt{1-\frac{K}{k_0}})\frac{e^{ik_0|z|\sqrt{1-\frac{K}{k_0}}}}{\sqrt{1-\frac{K}{k_0}}}$$

$$B_n^{(h)} = \frac{1}{i^n}(n,1;1,0\,|\,n,1)c_{n,1}P_n^1(\sqrt{1-\frac{K}{k_0}})e^{i\phi}\frac{e^{ik_0|z|\sqrt{1-\frac{K}{k_0}}}}{\sqrt{1-\frac{K}{k_0}}} \qquad (26)$$

$$C_n^{(h)} = \frac{-1}{i^{n+1}}(n,2;1,-1\,|\,n,1)c_{n,2}P_n^2(\sqrt{1-\frac{K}{k_0}})e^{2i\phi}\frac{e^{ik_0|z|\sqrt{1-\frac{K}{k_0}}}}{\sqrt{1-\frac{K}{k_0}}}$$

and

$$A_n^{(e)} = \frac{-1}{i^{n-1}}\left[\begin{array}{l}\sqrt{\frac{n+1}{2n+1}}(n-1,0;1,1\,|\,n,1)c_{n-1,0}P_{n-1}^0(\sqrt{1-\frac{K}{k_0}})\\[2mm]+\sqrt{\frac{n}{2n+1}}(n+1,0;1,1\,|\,n,1)c_{n+1,0}P_{n+1}^0(\sqrt{1-\frac{K}{k_0}})\end{array}\right]\frac{e^{ik_0|z|\sqrt{1-\frac{K}{k_0}}}}{\sqrt{1-\frac{K}{k_0}}}$$

$$B_n^{(e)} = \frac{i}{i^{n-1}}\left[\begin{array}{l}\sqrt{\frac{n+1}{2n+1}}(n-1,1;1,0\,|\,n,1)c_{n-1,1}P_{n-1}^1(\sqrt{1-\frac{K}{k_0}})\\[2mm]+\sqrt{\frac{n}{2n+1}}(n+1,1;1,0\,|\,n,1)c_{n+1,1}P_{n+1}^1(\sqrt{1-\frac{K}{k_0}})\end{array}\right]e^{i\phi}\frac{e^{ik_0|z|\sqrt{1-\frac{K}{k_0}}}}{\sqrt{1-\frac{K}{k_0}}} \qquad (27)$$

$$C_n^{(e)} = \frac{-1}{i^{n-1}}\left[\begin{array}{l}\sqrt{\frac{n+1}{2n+1}}(n-1,2;1,-1\,|\,n,1)c_{n-1,2}P_{n-1}^2(\sqrt{1-\frac{K}{k_0}})\\[2mm]+\sqrt{\frac{n}{2n+1}}(n+1,2;1,-1\,|\,n,1)c_{n+1,2}P_{n+1}^2(\sqrt{1-\frac{K}{k_0}})\end{array}\right]e^{2i\phi}\frac{e^{ik_0|z|\sqrt{1-\frac{K}{k_0}}}}{\sqrt{1-\frac{K}{k_0}}}$$

In this notation, the scattered field is finally expressed:

$$\mathbf{E}_{\text{scat}}(r_{//},\phi,z) = E_0\int_0^\infty \frac{K}{k_0}d\frac{K}{k_0}\left[\begin{array}{l}A(\frac{K}{k_0},\phi,z)J_0(Kr_{//})\frac{\{\hat{\mathbf{x}}+i\hat{\mathbf{y}}\}}{\sqrt{2}}\\[2mm]B(\frac{K}{k_0},\phi,z)J_1(Kr_{//})\hat{\mathbf{z}}\\[2mm]C(\frac{K}{k_0},\phi,z)J_2(Kr_{//})\frac{\{\hat{\mathbf{x}}-i\hat{\mathbf{y}}\}}{\sqrt{2}}\end{array}\right] \text{ with } \begin{array}{l}A = \sum_{n=0}^\infty f_n^{(h)}A_n^{(h)} + f_n^{(e)}A_n^{(e)}\\[2mm]B = \sum_{n=0}^\infty f_n^{(h)}B_n^{(h)} + f_n^{(e)}B_n^{(e)}\\[2mm]C = \sum_{n=0}^\infty f_n^{(h)}C_n^{(h)} + f_n^{(e)}C_n^{(e)}\end{array} \quad (28)$$

Acknowledgments